



Study of fluid cell coarsening for CFD-DEM simulations of polydisperse gas–solid flows

He Lei, Litao Zhu, Zhenghong Luo*

Department of Chemical Engineering, School of Chemistry and Chemical Engineering, State Key Laboratory of Metal Matrix Composites, Shanghai Jiao Tong University, Shanghai, 200240, China



ARTICLE INFO

Article history:

Received 20 March 2022

Received in revised form

29 April 2022

Accepted 3 May 2022

Available online 13 May 2022

Keywords:

Fluidized bed

CFD-DEM

Gas–solid flows

Fluid cell coarsening

Polydisperse drag force

ABSTRACT

Particle polydispersity is ubiquitous in industrial fluidized beds, which possesses a significant impact on hydrodynamics of gas–solid flow. Computational fluid dynamics–discrete element method (CFD-DEM) is promising to adequately simulate gas–solid flows with continuous particle size distribution (PSD) while it still suffers from high computational cost. Corresponding coarsening models are thereby desired. This work extends the coarse-grid model to polydisperse systems. Well-resolved simulations with different PSDs are processed through a filtering procedure to modify the gas–particle drag force in coarse-grid simulations. We reveal that the drag correction of individual particle exhibits a dependence on filtered solid volume fraction and filtered slip velocity for both monodisperse and polydisperse systems. Subsequently, the effect of particle size and surrounding PSD is quantified by the ratio of particle size to Sauter mean diameter. Drag correction models for systems with monodisperse and continuous PSD are developed. A priori analysis demonstrates that the developed models exhibit reliable prediction accuracy.

© 2022 Chinese Society of Particuology and Institute of Process Engineering, Chinese Academy of Sciences. Published by Elsevier B.V. All rights reserved.

1. Introduction

Gas–solid fluidized beds are widely used in various industrial processes, such as fluid catalytic cracking, olefin polymerization and coal gasification. The particles involved in these applications generally exhibit polydisperse characteristics with a continuous particle size distribution (PSD). With the addition of fines, particles size disparity affects the quality of fluidization (Geldart et al., 1981). Sun and Grace (1990) investigated the effect of the PSD in a catalytic fluidized bed. They revealed that the PSD has a profound impact on flow and mass transfer characteristics. Besides, polydispersity inevitably brings about mixing/separation issues, which have been explored by many experimental studies (Joseph et al., 2007; Wu & Baeyens, 1998). Nowadays, with the development of computational hardware and algorithms, the application of numerical simulation methods to deeply understand the complex behaviors inside fluidized beds has become increasingly popular. However, most studies have focused on monodisperse gas–particle flows (Gao, Li, & Rogers, 2018; Lei, Zhu, & Luo, 2021; Zhu et al., 2020, 2021), and

ignoring the PSD may lead to considerable deviations of the prediction.

Due to the indispensability of particle polydispersity, studies on modeling polydisperse systems have developed rapidly via different numerical methods such as the direct numerical simulation (DNS) (Seyed-Ahmadi & Wachs, 2020), multi-fluid model (MFM) (Xue & Fox, 2014) and Computational fluid dynamics–discrete element method (CFD-DEM) (Di Renzo et al., 2011; Zhang et al., 2017; Lan et al., 2020, 2021; Li et al., 2022). Firstly, the most precise technique is DNS, which can provide extremely detailed flow field information (Rong et al., 2014; van der Hoef et al., 2005). Van der Hoef et al. (2005) implemented lattice-Boltzmann simulations of bidisperse systems with different particle size ratios, and first constructed a drag correlation suitable for bidisperse systems. Rong et al. (2014) assembled an improved drag formula of bidisperse systems using more extensive data, and further generalized the equation to polydisperse systems. Nonetheless, due to high computational cost, most DNS studies are limited to the systems containing a few thousand particles. More importantly, the majority of these models are based on nearly homogeneous systems, while the effect of heterogeneity of particle concentration needs to be further considered in the application of coarse-grid simulations

* Corresponding author.

E-mail address: luozh@sjtu.edu.cn (Z. Luo).

(Sundaresan et al., 2018). Secondly, the computational overhead of MFM that is extended from two-fluid model (TFM) is much lower than that of DNS. So far, there are two most popular methods of coarse-grid MFM simulations, i.e., the filtered model (Holloway & Sundaresan, 2014; Lei, Liao, et al., 2021) and the Energy Minimization Multi-Scale (EMMS) model (Qin et al., 2019; Zhou & Wang, 2015). Holloway and Sundaresan (2014) performed fine-grid MFM simulations to investigate the filtered fluid-particle drag, particle-particle drag and particle phase stress in bidisperse systems. Zhou and Wang (2015) constructed the EMMS drag model for bidisperse systems, which was then verified in MFM simulations. Nevertheless, the kinetic theory of granular flow and particle-particle drag model applicable to polydisperse systems are still needed to close the interaction of particles. Moreover, a separate set of transport equations is required for each additional particle phase. Accordingly, it is commonly merely assumed that the mixture is approximately composed of particles with two or three particle sizes or densities. However, in most of industrial applications the practical mixtures exhibit a continuous PSD (Tirapelle et al., 2022). Thirdly, the computational cost of CFD-DEM is somewhere in between the MFM and DNS. The former directly tracks the movement of each particle through Newton's second law of motion. The contact force between particles can be resolved via a hard-sphere or soft-sphere model (Zhu et al., 2007). No extra physical model complexity is introduced for continuous PSD systems (Lu et al., 2018). Consequently, the CFD-DEM has a great potential in studying the effect of PSD.

Despite the advantages above, the computational resources required to perform CFD-DEM simulations of industrial scale devices are still unaffordable. Numerous studies have devoted to reducing its computational cost. On the one hand, to circumvent the issue of enormous number of particles, a group of real particles are lumped into a computational parcel, i.e., the coarse-grained particle method (CGPM). The CGPM has been developed rapidly in the last decade (Di Renzo et al., 2021; Wang & Shen, 2022) and extended to polydisperse systems by Chu et al. (2016) and Verma et al. (2017). Both studies lumped the identical-size particles into a representative parcel, resulting in similar PSDs. Different from the above studies, Lu et al. (2018) developed a CGPM that coarsens the polydisperse particles into a coarse monodisperse system and compared the advantages of different coarse graining strategies. Furthermore, with the rapid advancement of Graphical Processing Units (GPU), the capabilities in computing particle dynamics can be remarkably improved (Gan et al., 2016; Jajcevic et al., 2013; Xu et al., 2011). On the other hand, the gas phase model is usually solved by the CFD code with multiple Central Processing Units (CPU) (Jajcevic et al., 2013). Since the typical fluid cell size of CFD-DEM is equivalent to several particle sizes, simulations of industrial scale devices will inevitably lead to an astonishing number of grids, correspondingly requiring hundreds or even thousands of CPUs. Fortunately, fluid cell coarsening can considerably reduce the computational cost due to fluid computation. Meanwhile, particles coarsening generally should be accompanied by fluid cell coarsening since a fluid cell must contain a reasonable number of particles to ensure the accuracy of statistics (Ozel et al., 2016). Therefore, fluid cell coarsening is beneficial to promote the application of CFD-DEM simulations to larger scale devices.

Similar to coarse-grid continuum models, the corrections should be employed in coarse-grid CFD-DEM simulations to account for the effects of unresolved sub-grid scale structures (Benyahia & Sundaresan, 2012). Radl and Sundaresan (2014) assembled a filtered drag correction model for fluid cell coarsening through well-resolved CFD-DEM simulations. Ozel et al. (2016) performed fine-grid CFD-DEM simulations in a much larger domain to examine coarsening of both the fluid cell and

particle. It was indicated that the drag correction is almost entirely due to the fluid cell coarsening while the effect of the particle coarsening is weaker. Yu et al. (2020) developed a new sub-grid drag model for coarse-grid CFD-DEM simulations, which exhibited a better prediction performance in a prior analysis. In summary, the aforementioned studies have been focused on monodisperse systems. Although CFD-DEM approach is convenient for considering the PSD, to the best of our knowledge, there are few studies on grid coarsening of CFD-DEM simulations for bidisperse or even polydisperse gas-particle flows. This motivates us to develop a polydisperse sub-grid drag model for coarse-grid CFD-DEM simulations of gas-solid flows with a continuous PSD.

As a starting point, this work extends the studies on coarse-grid CFD-DEM drag models to the particle systems with general continuous PSDs. Firstly, well-resolved CFD-DEM simulations of gas-solid flows with typical PSDs are implemented. The effect of particle polydispersity on flow properties is evaluated in detail. Then, the drag correction of individual particle is extracted by filtering the simulation results at different filter sizes. The dependence of the drag correction on fluid and particle variables is investigated and the corresponding drag correction models for both monodisperse and polydisperse systems are constructed. The article is divided into the following sections: Sections “Mathematical modeling” and “Filtering procedure” present the mathematical model of CFD-DEM and filtering procedure, respectively. After that, the simulation settings are demonstrated in Section “Simulation settings”, and Section “Results and discussion” presents a detailed analysis and discussion of the simulation results. Finally, the principal conclusions of this study are summarized in the last section.

2. Mathematical modeling

In CFD-DEM simulations, the gas phase is described by the volume-averaged Navier-Stokes equations. The mass and momentum conservation equations are given by (Deen et al., 2007; Hou et al., 2019; Zhu et al., 2007)

$$\frac{\partial}{\partial t}(\rho_g \phi_g) + \nabla \cdot (\rho_g \phi_g \mathbf{u}_g) = 0 \quad (1)$$

$$\frac{\partial}{\partial t}(\rho_g \phi_g \mathbf{u}_g) + \nabla \cdot (\rho_g \phi_g \mathbf{u}_g \mathbf{u}_g) = -\phi_g \nabla p_g + \phi_g \nabla \cdot \boldsymbol{\tau}_g - \frac{\sum_{i \in \text{cell}} \mathbf{F}_{d,i}}{V_{\text{cell}}} + \rho_g \phi_g \mathbf{g} \quad (2)$$

where ρ_g , ϕ_g , \mathbf{u}_g and p_g denote the density, volume fraction, velocity and pressure of the gas phase, respectively. The gas phase stress tensor is denoted as $\boldsymbol{\tau}_g = \mu_g^* (\nabla \mathbf{u}_g + \nabla \mathbf{u}_g^T - \frac{2}{3} \nabla \mathbf{u}_g \cdot \mathbf{I})$. μ_g^* and \mathbf{I} are the effective gas phase viscosity and the unit matrix. $\mathbf{F}_{d,i}$ is the drag force acting on particle i . V_{cell} denotes the volume of the computational cell. \mathbf{g} is the gravitational acceleration.

The movement of each particle is tracked via Newton's second law of motion. The equations for translational and rotational motion of particle i are formulated as

$$m_i \frac{d\mathbf{v}_i}{dt} = -V_i \nabla p_{g,i} + \mathbf{F}_{d,i} + m_i \mathbf{g} + \sum_{\forall j \in \text{contact list}} (\mathbf{F}_{ij,n} + \mathbf{F}_{ij,t}) \quad (3)$$

$$I_i \frac{d\boldsymbol{\omega}_i}{dt} = \sum_{\forall j \in \text{contact list}} (R_i \mathbf{n}_{ij} \times \mathbf{F}_{ij,t}) + \sum_{\forall j \in \text{contact list}} \mathbf{M}_{ij,r} \quad (4)$$

where m_i , \mathbf{v}_i , V_i , ω_i and I_i represent the mass, velocity, volume, angular velocity and moment of inertia ($I_i = \frac{2}{5}m_i R_i^2$ for spherical particles with radius R_i) of particle i . On the right-hand side of Eq. (4), the terms respectively represent the fluid pressure gradient, drag, gravity and total contact forces. \mathbf{n}_{ij} is the unit vector in normal direction.

The soft sphere model (Cundall & Strack, 1979) is adopted to calculate the contact forces on particle i . The interparticle normal contact force is calculated as

$$\mathbf{F}_{ij,n} = \frac{4}{3}E^* \sqrt{R^*} \delta_n^{3/2} \mathbf{n}_{ij} + 2\sqrt{\frac{5}{6}} \zeta \sqrt{S_n m^*} \mathbf{v}_n^{rel} \quad (5)$$

where the equivalent Young's modulus, equivalent radius and equivalent mass are defined as $\frac{1}{E^*} = \frac{(1-\nu_i^2)}{E_i} + \frac{(1-\nu_j^2)}{E_j}$, $\frac{1}{R^*} = \frac{1}{R_i} + \frac{1}{R_j}$ and $\frac{1}{m^*} = \frac{1}{m_i} + \frac{1}{m_j}$, respectively. E_i , ν_i , R_i , m_i and E_j , ν_j , R_j , m_j are the Young's modulus, Poisson's ratio, radius and mass of particles i , j , respectively. δ_n and \mathbf{v}_n^{rel} denote the normal overlap and the normal component of the relative velocity. The damping coefficient is defined as $\zeta = \frac{\ln e}{\sqrt{\ln^2 e + \pi^2}}$ and the normal stiffness is determined by $S_n = 2E^* \sqrt{R^*} \delta_n$, where e denotes the coefficient of restitution.

The interparticle tangential contact force is given as

$$\mathbf{F}_{ij,t} = \begin{cases} -8G^* \sqrt{R^*} \delta_t \mathbf{t}_{ij} + 2\sqrt{\frac{5}{6}} \zeta \sqrt{S_t m^*} \mathbf{v}_t^{rel}, & \text{if } |\mathbf{F}_{ij,t}| \leq \mu_s |\mathbf{F}_{ij,n}| \\ -\mu_s |\mathbf{F}_{ij,n}| \mathbf{t}_{ij}, & \text{if } |\mathbf{F}_{ij,t}| > \mu_s |\mathbf{F}_{ij,n}| \end{cases} \quad (6)$$

where δ_t , \mathbf{v}_t^{rel} , μ_s and \mathbf{t}_{ij} denote the tangential overlap, the tangential component of the relative velocity, the particle sliding friction coefficient and the unit vector in the tangential direction, respectively. The tangential stiffness is defined as $S_t = 8G^* \sqrt{R^*} \delta_t$, where G^* is the equivalent shear modulus calculated by $\frac{1}{G^*} = \frac{(1-\nu_i)}{G_i} + \frac{(1-\nu_j)}{G_j}$.

The torques result from the rolling friction can be determined by $\mathbf{M}_{ij,r} = -\mu_{roll} |\mathbf{F}_{ij,n}| \frac{\omega_{rel}}{|\omega_{rel}|} R^*$ (Zhou et al., 1999). Where μ_{roll} is the coefficient of rolling resistance and ω_{rel} is the relative angular velocity between particle i and particle j .

In the present study, the Rong drag model (Rong et al., 2014) for polydisperse gas–solid flows, which is derived from LBM simulations, is employed to calculate the fluid–particle drag force on individual particles.

$$\mathbf{F}_{d,i}(\varphi_g, \mathbf{u}_{g,i} - \mathbf{v}_i, d) = \frac{1}{8} C_{d0}(Re) \pi \rho_g \alpha(\varphi_g, d) d_i d |\mathbf{u}_{g,i} - \mathbf{v}_i| \times (\mathbf{u}_{g,i} - \mathbf{v}_i) \varphi_g^{2-\beta(\varphi_g, Re)} \quad (7)$$

where $C_{d0}(Re)$, $\alpha(\varphi_g, d)$ and $\beta(\varphi_g, Re)$ are calculated respectively as

$$C_{d0} = \left(0.63 + \frac{4.8}{\sqrt{Re}}\right)^2 \quad (8)$$

$$\alpha(\varphi_g, d) = \frac{0.5 \varphi_g}{\sum_{i=1}^N \left(x_i / y_i^2\right)} + 0.5(1 - \varphi_g) y_i^2 + 0.5 y_i \quad (9)$$

$$\beta(\varphi_g, Re) = 2.65(1 + \varphi_g) - (5.3 - 3.5 \varphi_g) \varphi_g^2 \exp \left[-\frac{1}{2}(1.5 - \log Re)^2 \right] \quad (10)$$

$$y_i = \frac{d_i}{d}, \quad Re = \frac{\varphi_g d |\mathbf{u}_{g,i} - \mathbf{v}_i| \rho_g}{\mu_g^*}, \quad d = \frac{\sum_{i=1}^N d_i^3}{\sum_{i=1}^N d_i^2}, \quad x_i = \frac{\varphi_i}{1 - \varphi_g} \quad (11)$$

where d_i , d , Re and x_i denote the diameter of particle i , Sauter mean diameter, particle Reynolds number and mass fraction of particles i , respectively. The fluid variables ($\mathbf{u}_{g,i}$ and $\nabla p_{g,i}$) at the position of particle i are obtained by linear interpolation.

Properties of particles are mapped to fluid cell via the method of satellite point (Clarke et al., 2018), which assumes multiple randomly distributed pseudo-particles to represent a real particle. The volume fraction of particle i and the voidage in the fluid cell is calculated by:

$$\varphi_i = \frac{\psi_i V_i}{V_{cell}} \quad (12)$$

$$\varphi_g = 1 - \sum_{i \in cell} \varphi_i \quad (13)$$

here, the volume fraction of a particle i in the specific cell is $\psi_i = \frac{N_{i,cell}}{N_{i,total}}$, where $N_{i,total}$ is the total number of the pseudo-particles constitute the particle i and $N_{i,cell}$ is the part within the cell.

3. Filtering procedure

The correction to the fluid–particle drag force is deduced by implementing a filtering procedure on the well-resolved simulation results. Analogous to monodisperse systems (Ozel et al., 2016; Radl & Sundaresan, 2014; Yu et al., 2020), the filtering strategy for polydisperse gas–solid flows is carried out here. The filtered fluid and particle phase volume fraction at the center of each filtered region are defined as:

$$\bar{\varphi}_g(\mathbf{x}, t) = \iiint \varphi_g(\mathbf{r}, t) G(\mathbf{r} - \mathbf{x}) d\mathbf{r} \quad (14)$$

$$\bar{\varphi}_s(\mathbf{x}, t) = 1 - \bar{\varphi}_g(\mathbf{x}, t) \quad (15)$$

where $G(\mathbf{r} - \mathbf{x})$ is a weight function satisfying $\iiint G(\mathbf{r}) d\mathbf{r} = 1$. The box filter kernel adopted in the present study is given by

$$G(\mathbf{r} - \mathbf{x}) = \begin{cases} \frac{1}{\Delta_f^3}, & \text{if } |\mathbf{r} - \mathbf{x}| \leq \frac{\Delta_f}{2} \\ 0, & \text{otherwise} \end{cases} \quad (16)$$

The filtered velocity of the gas at the center of each filtered region is defined as

$$\tilde{\mathbf{u}}_g(\mathbf{x}, t) = \frac{1}{\bar{\varphi}_g} \iiint G(\mathbf{r} - \mathbf{x}) \bar{\varphi}_g(\mathbf{r}, t) \mathbf{u}_g(\mathbf{r}, t) d\mathbf{r} \quad (17)$$

As the detailed structure of fluid flow is unresolved in the coarse-grid CFD–DEM simulations, the fluid–particle drag on each particle in the vertical direction (indicated by subscript z) is generally calculated based on the filtered fluid variables as follows (Yu et al., 2020):

$$\begin{aligned} \tilde{\mathbf{F}}_{d,i,z}(\tilde{\varphi}_{g,i}, \tilde{\mathbf{u}}_{g,i,z} - \mathbf{v}_{i,z}, \tilde{d}) &= \frac{1}{8} C_{d0}(\tilde{Re}) \pi \rho_g \alpha(\tilde{\varphi}_{g,i}, \tilde{d}) \tilde{d}_i \tilde{d} |\tilde{\mathbf{u}}_{g,i,z} - \mathbf{v}_{i,z}| \\ &\times (\tilde{\mathbf{u}}_{g,i,z} - \mathbf{v}_{i,z}) \frac{2 - \beta(\tilde{\varphi}_{g,i}, \tilde{Re})}{\tilde{\varphi}_{g,i}} \end{aligned} \quad (18)$$

where the filtered volume fraction $\tilde{\varphi}_{g,i}$ and velocity $\tilde{\mathbf{u}}_{g,i,z}$ of gas phase are interpolated at the position of particle i (Radl & Sundaresan, 2014). The calculation of $C_{d0}(\tilde{Re})$, $\alpha(\tilde{\varphi}_{g,i}, \tilde{d})$ and $\beta(\tilde{\varphi}_{g,i}, \tilde{Re})$ are respectively according to Eqs. (8)–(10). The filtered Reynolds number and Sauter mean diameter are defined as $\tilde{Re} =$

$$\frac{\tilde{\varphi}_{g,i} \tilde{d} |\tilde{\mathbf{u}}_{g,i,z} - \mathbf{v}_{i,z}| \rho_g}{\mu_g}, \quad \tilde{d} = \frac{\sum_{i=1}^{N_{filter}} d_i^3}{\sum_{i=1}^{N_{filter}} d_i^2}.$$

The drag force determined in the well-resolved CFD-DEM simulations is regarded as the standard value. The correction to the coarse-grid drag force is defined as the ratio of the filtered drag force of individual particles to the corresponding term in the fine-grid simulations, and is given as follows

$$H_{d,i} = \frac{\mathbf{F}_{d,i,z}(\varphi_g, \mathbf{u}_{g,i,z} - \mathbf{v}_{i,z}, d)}{\tilde{\mathbf{F}}_{d,i,z}(\tilde{\varphi}_{g,i}, \tilde{\mathbf{u}}_{g,i,z} - \mathbf{v}_{i,z}, \tilde{d})} \quad (19)$$

4. Simulation settings

The principal parameters including the settings of the simulation domain size, fluid and particle properties are summarized in Table 1. The 3D rectangular domain consists of a bottom velocity inlet, a top pressure outlet, and four periodic boundary sides. Moreover, the top of the domain is set as a fictitious wall to avoid particles escaping from the bed. In order to examine the effect of particle polydispersity, four different PSDs are set up as presented in Fig. 1. Case I is a monodisperse system with a particle diameter of 80 μm . The PSD of Case II is taken from the experimental data of Wang (2013). It should be noted that the particles with a diameter of less than 40 μm are not considered due to strong cohesion between particles, which is not the objective of this work. In comparison, Case III has a narrower PSD and Case IV has a larger particle size with a PSD curve similar to that of Case II. The particle size range, Sauter mean diameter, specific particle number and gas velocity of each case are given in Table 2. The typical fluid cell size of CFD-DEM is several times of the average particle sizes (Zhao &

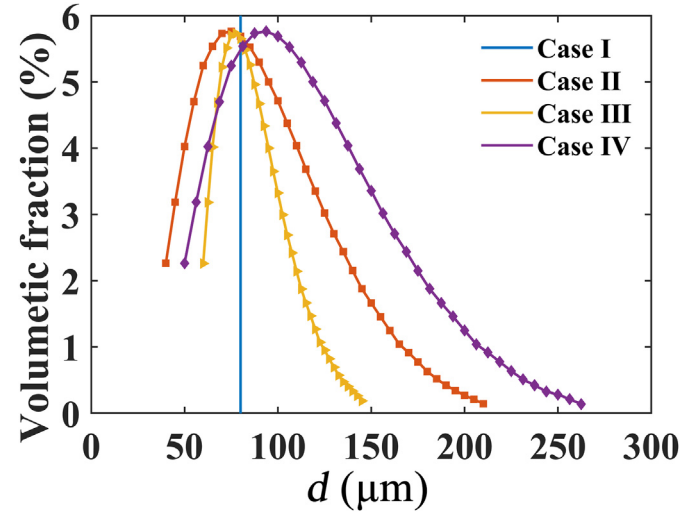


Fig. 1. Particle size distributions (PSDs) of Cases I–IV. Case I is monodisperse. Each polydisperse case (Case II, III, IV) contains 35 different particle sizes.

Shan, 2013). For convenience, the fluid grid size in this work is uniformly chosen to be 400 μm , which is 4–5 times the average particle size and 1.5 times the maximum particle size. The method of satellite point (Clarke et al., 2018) is employed to ensure the accuracy of the volume fraction calculation. The initial particle volume fraction of the domain is 0.1. All simulations are run in advance to reach a pseudo-steady state. Then, for Case I, we filtered the snapshots within $10 \tau_p^{St}$ (the Stokes relaxation time of the particle is defined as $\tau_p^{St} = \frac{\rho_p d^2}{18 \mu_g} = 0.0296 \text{ s}$) to collect sufficient data. The same processing is applied to the remaining cases. The effective gas phase viscosity is set equal to the molecular viscosity (Agrawal et al., 2013).

5. Results and discussion

The volume fraction of particles with different sizes in each case is shown in Fig. 1. Each polydisperse case (Case II, III, IV) contains 35 different particle sizes, which is comparable to continuous PSD. The particles involve Geldart types A and B particles and the particle size ranges from 40 μm to 263 μm . Overall, the cases with four different PSDs are designed to achieve the purpose of this study.

Snapshots of the particle flow in different cases are shown in Fig. 2. Particles are colored according to its diameter. The observed segregation of particles is due to the wide variations in drag forces acting on particles with different sizes. It is evident that small particles tend to disperse at the top part of the bed. Particle cluster structures can be clearly found in the 2D cross-sectional view. Besides, local gas properties such as gas velocity show obvious inhomogeneity. In fine-grid simulations, the local properties of the fluid phase are well resolved. Nonetheless, with the coarsening of the grid, the locally heterogeneous fluid structures in the coarse grid are unresolved. The drag force for each particle is calculated based on the gas velocity of the cell where the particle is located. This inevitably leads to deviations in fluid-particle drag calculations. Further insight into this issue will be discussed later in this section.

The evolution of the average axial height for particles are presented in Fig. 3. The particles with different sizes have almost the same initial average height since the particles are randomly generated. In the beginning ($t < 0.05 \text{ s}$), the average height of all the particles keeps dropping due to a low gas velocity of 0.1 m/s.

Table 1

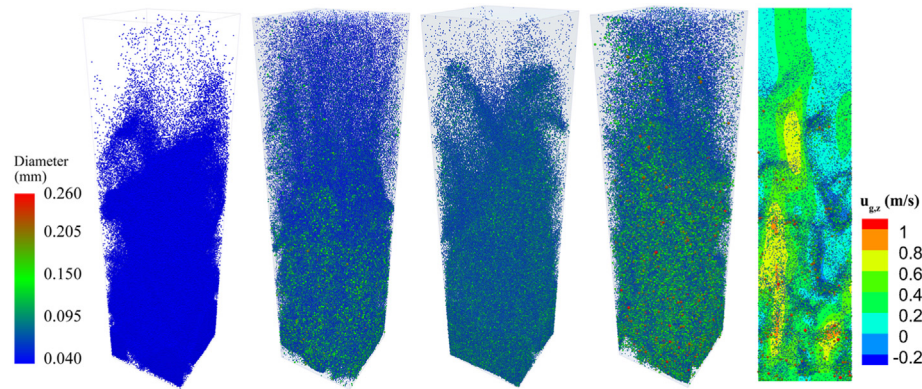
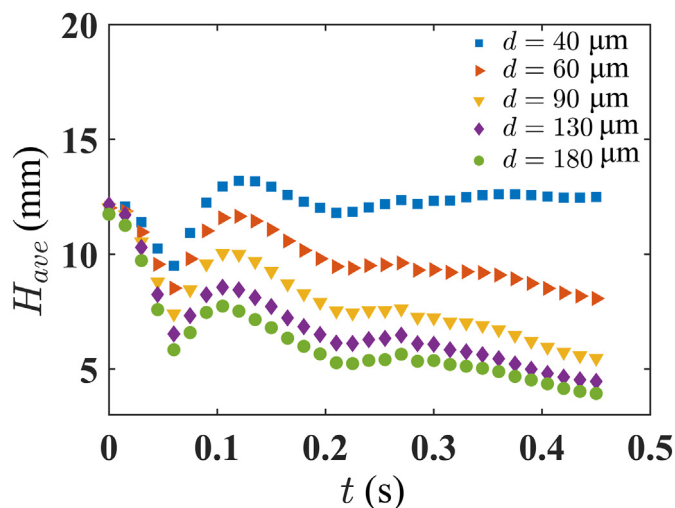
The computational domain and simulation parameters.

Simulation parameters	Value
Particle diameter, d (μm)	40–263
Domain size (mm)	$8 \times 8 \times 32$
Grid size (μm)	$400 \times 400 \times 400$
Acceleration due to gravity, \mathbf{g} (m/s^2)	−9.81
Particle density, ρ_p (kg/m^3)	1500
Young's modulus, E (Pa)	10^6
Poisson's ratio, ν	0.42
Restitution coefficient, e	0.9
Particle–particle friction coefficient, μ_p	0.4
Rolling friction coefficient, μ_{roll}	0.1
Gas density, ρ_g (kg/m^3)	1.3
Gas molecular viscosity, μ_g (kg/(m s))	1.8×10^{-5}
Filter size, d	9–50
DEM time step (s)	1×10^{-6}
Fluid time step (s)	1×10^{-5}

Table 2

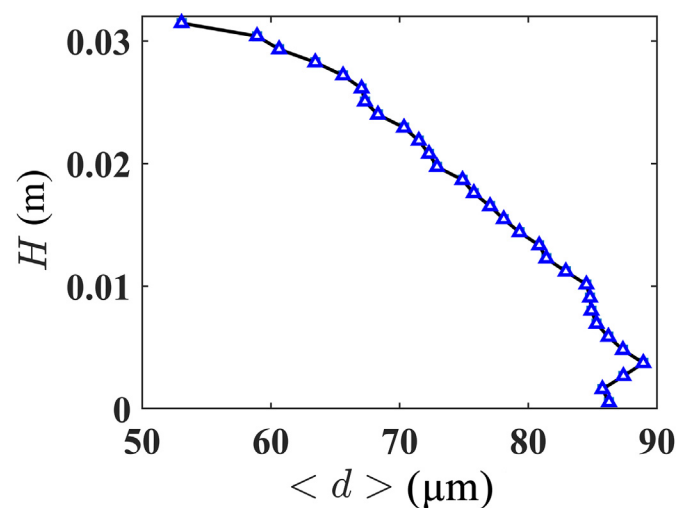
A list of initial particle size distributions, total number of particles performed and gas velocities in this study.

Case	Particle diameter, d (μm)	Sauter mean diameter, d (μm)	Total number of particles, N_{total} ($\times 10^4$)	Gas velocity, u_g (m/s)
I	80	80	76	0.1–0.15
II	40–210	82.8	102	0.1–0.15
III	60–145	84.5	73	0.1–0.15
IV	50–263	103.5	52	0.15–0.2

**Fig. 2.** Snapshots of the particle flow in different cases colored by particle diameter, from left to right are Case I, II, III, IV and 2D cross-sectional view of Case IV with axial gas velocity contour.**Fig. 3.** The evolution of the average axial height for particles of different sizes over time. The data is taken from Case II.

Subsequently, with the gas velocity increasing to 0.15 m/s at $t = 0.05$ s, the average height of the particles starts to increase. After that, the average bed height of small particles tends to stabilize over time, while that of the large particles slowly decrease. As time evolves, the gap between the average height of the different-size particles continues to increase. It is an indicator that the degree of particle segregation intensifies.

The variation of Sauter mean diameter along the bed height is shown in Fig. 4. It is demonstrated that the particle composition at the bottom of the bed is quite different from that at the top. The Sauter mean diameter of the cross-section generally decreases as the bed height increases. In short, Figs. 3 and 4 both indicate that the polydispersity of the particles inevitably affects the flow dynamics of the particles, which will further affect the mass and heat transfer performance of the reactor. Most of the traditional coarse-

**Fig. 4.** Variation of Sauter mean diameter with the height of the bed. The data is averaged in the statistic time from 0.18 s to 0.45 s.

grid model studies, especially for coarse-grid CFD-DEM, assume a monodisperse system, which cannot reflect these typical characteristics of a practical polydisperse system. A coarse-grid model for gas–solid flows with a continuous PSD is urgently needed.

As shown in the 2D cross-sectional view in Fig. 2, the fluid phase properties exhibit a remarkable inhomogeneity, which are locally averaged in the coarse-grid simulations. In numerous studies on coarse-grid TFM simulations of monodisperse gas–solid flows, it was shown that grid coarsening has a significant impact on the prediction of drag force (Agrawal et al., 2001; Sarkar et al., 2016; Zhu et al., 2019, 2020). Analogously, the correction to the drag force is also required for coarse-grid CFD-DEM simulations (Benyahia & Sundaresan, 2012; Radl & Sundaresan, 2014). In the following, we will implement a filtering strategy to evaluate the effect of fluid coarsening on the drag force in polydisperse systems. The obtained

drag correction can be then applied for coarse-grid CFD-DEM simulations.

It should be noted that the data of particles at the vicinity of the wall are abandoned to circumvent the influence of the wall (Rauchenzauner & Schneiderbauer, 2020). The distribution of drag corrections with the filtered particle volume fraction is presented in Fig. 5. Most drag corrections are between 0 and 2. The drag corrections greater than 4 are not taken into account in the statistics as it accounts for less than 1.0% of the dataset and its inclusion will significantly reduce the predictive performance of the correction model. Note that the resulting trend of the different cases are similar. Thus, only the results for Case II are presented as a representative of the polydisperse systems for the sake of conciseness. The figure indicates that grid coarsening has a vital influence on the drag force of individual particle, both for monodisperse (Fig. 5(a)) and polydisperse systems (Fig. 5(b)). Even when the filter size is 4 times the fine-grid size, the correction of drag force is not negligible. The value of $H_{d,i}$ less than 1 usually indicates that the drag force is overestimated in the coarse-grid model, and conversely underestimated when it is greater than 1. A larger deviation of the value of $H_{d,i}$ from 1 indicates that the coarse-grid drag force deviates greatly from the actual value. Moreover, it is noted that the drag correction depends on the filtered particle volume fraction. The average drag corrections binned by the filtered solid volume fraction are presented as triangles. Overall, the drag correction approaches unity with the filtered solid volume fraction tending to 0. As the filtered solid volume fraction increases, the drag correction first decreases until the filtered solid volume fraction exceeds 0.4 and then increases. Most drag corrections are distributed around the average value. Generally, drag corrections are regarded as an index of inhomogeneity within a grid cell. As the drag correction deviates from 1, the inhomogeneity within the cell increases. In previous studies of monodisperse systems (Ozel et al., 2016; Radl & Sundaresan, 2014), the drag corrections for coarse-grid CFD-DEM are usually quantified by the filter size and filtered particle volume fraction. Nevertheless, Fig. 5(a) shows that at a certain filter size and filtered particle volume fraction, there is a fairly wide distribution of the drag correction even for a monodisperse system. This phenomenon exists for polydisperse systems as well in Fig. 5(b). Therefore, it is necessary to reduce the prediction uncertainty, improve the predictive performance of monodisperse systems, and then further quantify the additional complexity introduced by polydispersity.

Studies on coarse-grid TFM simulations have pointed out that the filtered slip velocity can serve as an additional marker for the drag correction (Milioli et al., 2013). A similar investigation is implemented in the coarse-grid CFD-DEM simulations. There are two common definitions of filtered slip velocities for filtered CFD-

DEM studies in the literature, namely, the slip velocity of single particle (Radl & Sundaresan, 2014; Ozel et al., 2016) and the mass-averaged slip velocity of all particles in the filtered region (Yu et al., 2020). Considering that it is common to calculate the drag force with the velocity of a single particle in practical CFD-DEM simulations, the filtered slip velocity of single particle is thereby adopted in this study. For rendering the filtered slip velocity in a dimensionless form, we have examined the terminal velocity based on Stokes' law of the particle with a local Sauter mean diameter and with a single-particle diameter, respectively. Different from the monodisperse studies, the terminal velocity based on Stokes' law of

the particle itself $\tilde{u}_{slip,z,i}^* = \frac{|\tilde{u}_{slip,z}|}{v_{t,i}} = \frac{|\tilde{u}_{g,i,z} - v_{t,i}|}{v_{t,i}}$ is adopted since the drag correction has a much more pronounced dependence on the resulting dimensionless filtered slip velocity. The terminal velocity based on Stokes' law of the particle i is defined as $v_{t,i} = \frac{gd_p^2(\rho_s - \rho_g)}{18\mu_g}$. In

Fig. 6 it is apparent that the drag correction exhibits a dependence on the dimensionless filtered slip velocity at different filtered solid volume fractions. Especially when the dimensionless filtered slip velocity is in the range of 0–0.5, the drag correction decreases significantly with the increase of the filtered slip velocity. As the filtered slip velocity further increases, the variation in the drag correction becomes gentle, which indicates that the inhomogeneity within the cell has less fluctuations. We consider that a larger slip velocity generally corresponds to a larger degree of segregation between the gas and solid phases (Milioli et al., 2013). The segregation degree increases rapidly with increasing the slip velocity when the slip velocity is small, and it no longer changes significantly with the further increase of the slip velocity. In addition, for the dimensionless filtered slip velocity greater than 0.5, the drag force at a large filtered solid volume fraction (for example 0.45) is remarkably overestimated and corresponds to a value of $H_{d,i}$ much less than 1. It is reminiscent that for fluidized systems with a large particle concentration, coarse-grid simulations will significantly overestimate the bed expansion height, which has been observed in many works (Gao, Li, Sarkar, et al., 2018; Schneiderbauer et al., 2013). The quantitative relationship between the drag correction and the filtered slip velocity of polydisperse system (Case II) is shown in Fig. 6(b). We limit the particle size to the range of 75–85 μm , which is close to the size of monodisperse system of 80 μm . The comparison of Fig. 6(a) and (b) shows that the drag correction of the polydisperse system is analogous to that of the monodisperse system while there are quantitative differences.

The above results prove that the markers used for monodisperse systems are still applicable for continuous PSD systems. Recently, it has been found that the filtered pressure gradient can serve as an additional good marker since its inclusion can significantly improve

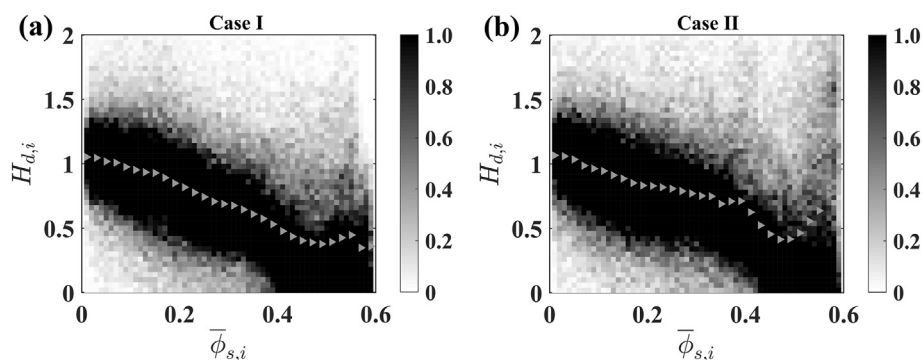


Fig. 5. The probability distribution of the drag corrections as a function of the filtered particle volume fraction. The filter size is 4 times of the fine-grid size. The triangle represents the average drag correction binned by the filtered solid volume fraction. (a) Case I, (b) Case II.

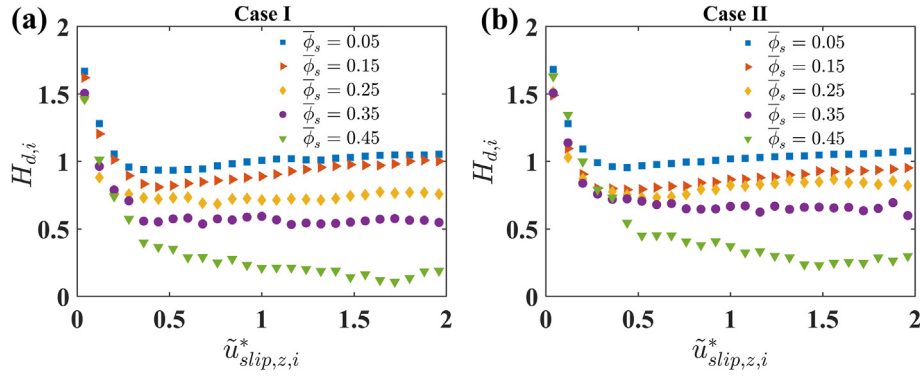


Fig. 6. The drag correction as a function of the dimensionless filtered slip velocity. The filter size is 4 times of the fine-grid size. (a) Case I, (b) Case II.

the prediction accuracy of the drag correction (Jiang et al., 2021; Zhu et al., 2020). However, there is no observable dependence of the drag correction on the fluid pressure gradient in our examination. This observation may be understood by the following clarification. Previous works have been devoted to developing the drag correction models for coarse-grid TFM (Jiang et al., 2021; Zhu et al., 2021) and they are based on the grid scale. This study is devoted to developing a drag correction model for coarse-grid CFD-DEM simulations and it is based on the particle scale. Moreover, in the studies of bidisperse gas–particle flows (Holloway et al., 2011; Holloway & Sundaresan, 2014; Lei, Liao, et al., 2021), it has been revealed that the drag correction for MFM simulations depends on the particle size ratio and volume fraction ratio. Meanwhile, from the drag model of Rong et al. (2014) for polydisperse systems, namely Eq. (7), it is noted that the drag force of individual particle in CFD-DEM simulations is correlated with the particle size itself and the particle size composition around in the computational cell. The grid coarsening will inevitably alter the composition of particles in the cell and thus affect the calculation of drag force. Consequently, in order to identify the characteristics of the polydisperse system, the correlation between the drag correction in polydisperse systems with the particle size and the composition of the particles in the cell are examined. Fig. 7 shows the drag

correction as a function of y_i (y_i is defined as the ratio of the particle diameter to the Sauter mean diameter of the cell $\frac{d_i}{d}$) at various filtered solid volume fractions. It is noteworthy that the results are obtained at the specified dimensionless filtered slip velocity of 0.2. The figure illustrates that for particles in a specified cell (corresponding to an identical Sauter mean diameter), the smaller particle requires a larger value of $H_{d,i}$. For particles with the same size, the particle with a smaller Sauter mean diameter corresponds to a smaller value of $H_{d,i}$. The possible argument is that the cell with a small Sauter mean diameter contains more small particles, generally tending to result in more heterogeneous structures. For different filtered solid volume fractions, the drag correction shows a consistent variation tendency with $\frac{d_i}{d}$.

The results of Fig. 7 are obtained at a specific dimensionless filtered slip velocity. Further investigation on the quantitative relationship between the drag correction and $\frac{d_i}{d}$ at different filtered slip velocities are shown in Fig. 8. It should be noted that the filtered solid volume fraction is a constant of 0.35. At a low dimensionless slip velocity (0.1 or 0.2), the drag correction is sensitive to the variation of $\frac{d_i}{d}$. Nevertheless, the dependence becomes less pronounced as the slip velocity increases. We argue that this may be due to the fact that when the slip velocity approaches or

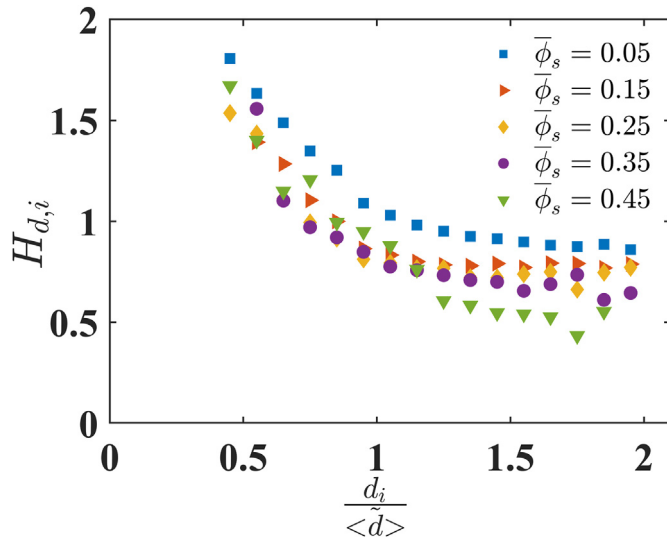


Fig. 7. The drag correction as a function of the $\frac{d_i}{d}$ at different filtered solid volume fractions. The results are obtained at a dimensionless filtered slip velocity of 0.2 of Case II. The filter size is 4 times of the fine-grid size.

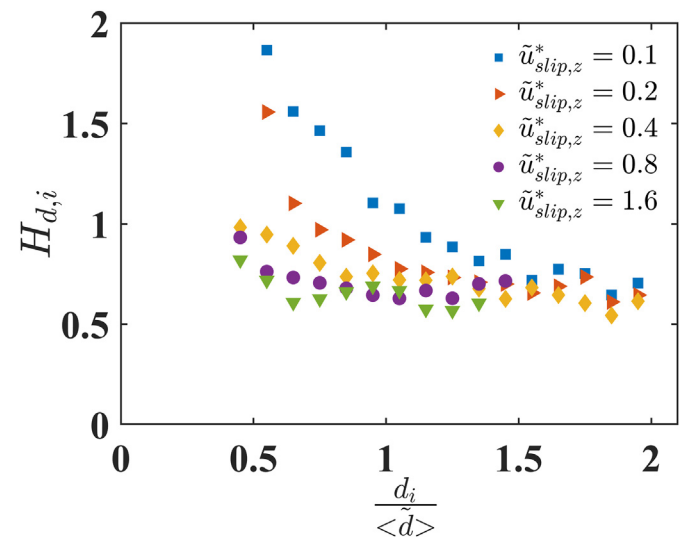


Fig. 8. The drag correction as a function of the $\frac{d_i}{d}$ at different filtered slip velocities. The results present are obtained at a filtered solid volume fraction of 0.35 of Case II. The filter size is 4 times of the fine-grid size.

even exceeds the particle terminal settling velocity, most of the particles are entrained by or flow with the airflow. As a result, the effect of particle composition on fluid inhomogeneity is diminished. To sum up, in polydisperse systems, the effect of the particle size and the surrounding PSD of the cell should be taken into account in the determination of the drag correction, particularly at low slip velocities. Correspondingly, a drag correction model for the coarse-grid CFD-DEM simulations of continuous PSD systems should be established.

Based on the above analysis, the filtered solid volume fraction and the dimensionless filtered slip velocity are determined as the closure markers of the drag correction for coarse-grid CFD-DEM simulations in monodisperse systems. The data obtained from Case I are binned according to the filtered solid volume fraction and dimensionless filtered slip velocity. The filtered solid phase volume fraction in the range of 0–0.6 are divided into 60 bins at a uniform interval of 0.01. The dimensionless filtered slip velocity in the range of 0–5 is divided into 50 bins at a uniform interval of 0.1. The drag corrections within each bin are averaged to obtain the averaged drag corrections for the specific filtered solid volume fraction and dimensionless filtered slip velocity. The filter size is dimensionless by the particle diameter in monodisperse systems. By fitting the data of five different filter sizes, the drag correction model of the monodisperse system is obtained as follows:

$$H_{d,i} = a\bar{\varphi}_{g,i}^b + c\bar{u}_{slip,z,i}^*{}^d + e\bar{u}_{slip,z,i}^*{}^f \quad (20)$$

The values of a–f at different filter sizes are listed in Table 3. The coefficient of the determination (R^2) and the mean absolute percentage error (MAPE) are employed to quantitatively evaluate the performance of the model. The definitions of R^2 and MAPE are as follows:

$$R^2 = 1 - \frac{\sum_{i=1}^N (y_{\text{exact}} - y_{\text{predict}})^2}{\sum_{i=1}^N (y_{\text{exact}} - \bar{y}_{\text{exact}})^2} \quad (21)$$

$$\text{MAPE} = \frac{1}{N} \sum_{i=1}^N \left| \frac{y_{\text{exact}} - y_{\text{predict}}}{y_{\text{exact}}} \right| \% \quad (22)$$

Subsequently, the simulation results of polydisperse Cases II–IV are processed and combined with Case I together. Analogous to the treatment in monodisperse systems, polydisperse data are first binned by the filtered solid volume fraction and dimensionless filtered slip velocity. In order to quantify the effect of particle size and PSD of polydisperse systems, each previous bin is further divided into 30 bins by $\frac{d_f}{d_i}$ in the range of 0.5–2 at a uniform interval of 0.05. The drag correction in each bin is averaged to obtain the filtered drag corrections for each specific filtered solid volume

fraction, dimensionless filtered slip velocity and $\frac{d_f}{d_i}$. It is worth noting that monodisperse data corresponding to $\frac{d_f}{d_i}$ equal to 1 are also take into account in the following fit. In this work, the cell size is 4–5 times the Sauter mean diameter of the systems. For the convenience of future applications, we uniformly take the average of the Sauter mean diameter of Cases I–IV in the Table 2 as the dimensionless standard for the filter size in polydisperse systems. The following model is recommended for use in the particle size range within the scope of this study. The drag correction model of gas–particle flow with general PSD at different filter sizes is obtained as follows:

$$H_{d,i} = a\bar{\varphi}_{g,i}^b \bar{u}_{slip,z,i}^*{}^c y_i + d\bar{u}_{slip,z,i}^*{}^e y_i^f + g\bar{u}_{slip,z,i}^*{}^h y_i^k \quad (23)$$

where $y_i = \frac{d_f}{d_i}$. The values of a–k at different filter sizes are listed in Table 4.

Furthermore, the predictive performance of the above models is evaluated in a priori analysis. Fig. 9 presents the comparison of the predicted filtered drag corrections versus the exact values. The monodisperse results with a filter size of 20 d_i in Fig. 9(a) show that most of the predicted values are distributed near the diagonal line, indicating that the proposed model could properly capture the variation of the drag correction. With the addition of the new marker $\frac{d_f}{d_i}$, Eq. (23) also exhibits good predictive performance for polydisperse systems in Fig. 9(b) at a dimensionless filter size of 18.2. Quantitative evaluation of the performance of the models at different filter sizes is given in Fig. 10. To the best of our knowledge, only the work of Yu et al. (2020) has quantitatively evaluated the predictive performance of drag correction models for coarse-grid CFD-DEM simulations in monodisperse systems. The R^2 at different filter sizes typically below 0.8. In this work, for the monodisperse system, when the filter size is 20 or 30 d_i , the R^2 exceeds 0.9 and the MAPE is below 10% in Fig. 10(a). This indicates that the proposed model ensures high prediction accuracy with the premise of simplicity. As the filter size increases to 40 and 50 d_i , the prediction accuracy of the model decreases. This observation in monodisperse systems is analogous to that in the work of Yu et al. (2020).

In Fig. 10(b), a similar phenomenon appears for continuous PSD systems, that is, the MAPE of the model within the filter size scope of this study is all less than 20%. When the dimensionless filter size is 18.2, the R^2 of the model reaches 0.8 and the MAPE is less than 10%. Due to the extra complexity associated with polydispersity, the prediction accuracy of the model is generally lower than that of the monodisperse system. But in general, the model still gives reasonable prediction accuracy for the dimensionless filter size is 18.2 or 27.4. It is worth mentioning that the grid number decreases by a power of 3 with the increase of the grid size. Therefore, the scope of the filter size studied in this work is able to reduce the number of the grid by hundreds of times. The recommended application range of grid size is 18–30 times the Sauter mean diameter of the system and the particle size range is preferable within the scope of this study. The predictive performance of the drag correction model decreases for large filter sizes. We argue that this is mainly because the resolution of the fluid phase is worse as the excessive coarsening of the grid. The gas phase properties at the particle locations in the coarse-grid simulation increasingly deviate from those in the fine-grid simulation, which in turn leads to a decrease in the accuracy of the calculation for drag force. On the other hand, with the coarsening of the grid, the interpolation method of the fluid phase properties at the particle position will

Table 3

A list of values of parameters a–f, the coefficient of determination (R^2) and the mean absolute percentage error (MAPE) in the drag correction model Eq. (20) of monodisperse systems at different filter sizes.

$\frac{\Delta_f}{d_i}$	a	b	c	d	e	f	R^2	MAPE (%)
10	−0.926	1.35	0.0167	−0.941	0.995	0.0414	0.8747	3.58
20	−1.93	1.30	0.624	−0.335	0.390	0.643	0.9394	7.66
30	−3.03	1.69	0.747	−0.301	0.241	1.17	0.9148	9.22
40	−11.2	3.20	0.768	−0.307	0.154	1.68	0.7976	12.57
50	−19.4	4.05	0.792	−0.311	0.112	1.69	0.6442	16.07

Note: $\frac{\Delta_f}{d_i}$ denotes the ratio of the filter size to the particle diameter.

Table 4

A list of values of parameters a–k, the coefficient of determination (R^2) and the mean absolute percentage error (MAPE) in the drag correction model Eq. (23) of polydisperse systems at different filter sizes.

$\frac{\Delta_f}{d}$	a	B	c	d	E	f	g	H	k	R^2	MAPE (%)
9.12	−3.13	2.75	0.571	0	0	0	0.989	0.0452	0.0278	0.7225	4.46
18.2	−3.22	1.89	0.538	0.235	−0.485	−0.935	0.771	0.306	0.480	0.8177	8.98
27.4	−2.66	1.61	0.636	0.368	0.921	1.55	0.657	−0.291	−0.615	0.7490	12.09
36.5	−2.82	1.69	0.686	0.244	1.38	2.32	0.787	−0.275	−0.603	0.6965	15.43
45.6	−3.18	1.92	0.703	0.857	−0.278	−0.628	0.143	1.95	3.27	0.6250	17.82

Note: $\frac{\Delta_f}{d}$ denotes the ratio of the filter size to the Sauter mean diameter. The average of the Sauter mean diameter of Cases I–IV is 87.7 μm .

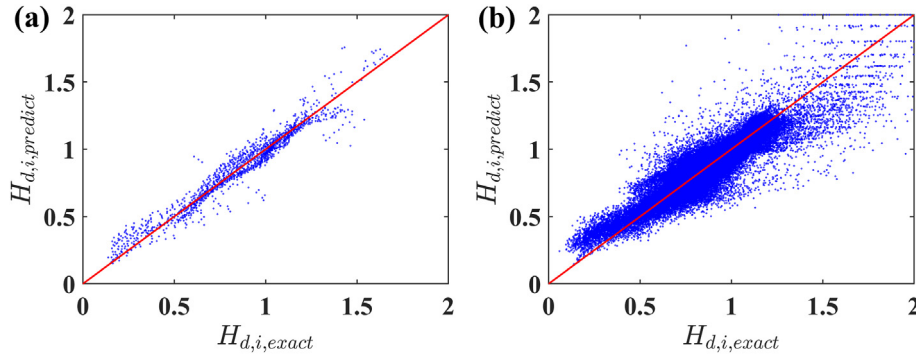


Fig. 9. Comparison of the predicted filtered drag corrections $H_{d,i,predict}$ versus exact values $H_{d,i,exact}$ of (a) monodisperse system (Case I) and (b) general PSD systems (Case I–IV). The dimensionless filter size is 20 and 18.2 for (a) and (b), respectively.

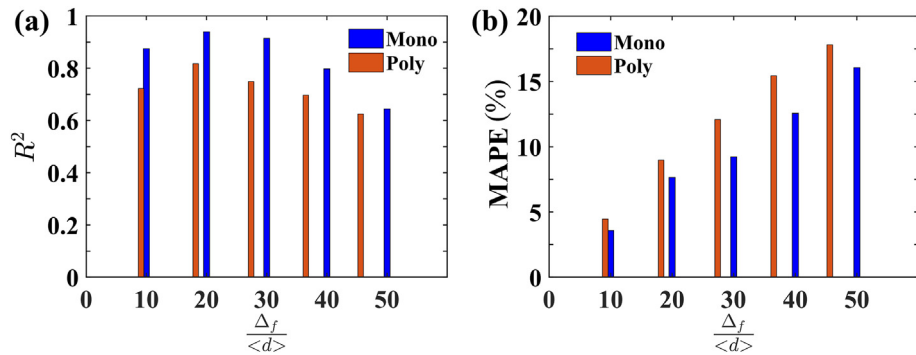


Fig. 10. The coefficient of determination (R^2) and the mean absolute percentage error (MAPE) as a function of the ratio of the filter size and the Sauter mean diameter $\frac{\Delta_f}{d}$ in (a) monodisperse system (Case I) and (b) general PSD systems (Cases I–IV).

also have a certain impact on the calculation of the drag force. Further research is needed.

As there are no studies on coarse-grid drag correction for polydisperse CFD-DEM simulations, here we only compare the monodisperse results with data from Radl and Sundaresan (2014) and Ozel et al. (2016), as shown in Fig. 11. The dimensionless filtered slip velocity used in Eq. (20) is the median of the data binned by the filtered solid volume fraction. The three models all illustrate that the drag force of individual particle is generally overestimated in the coarse-grid simulations. It is noted that there are differences between the three models. We argue that it is probably due to the different ranges of slip velocities studied in different works. Consequently, it is desirable to take into account the slip velocity or other suitable markers to more accurately predict the drag corrections. In addition, the drag correction data included in this work range from 0 to 4, which is not mentioned in the other two works. The value of $H_{d,i}$ greater than 1 still occupies a certain proportion especially at small solid concentrations. This may explain why the value of $H_{d,i}$ predicted by this work is larger

than the other models at small solid concentrations. Note that at large solid concentrations, the present model predicts a drag correction similar to that of Radl and Sundaresan (2014).

To date, substantial validation of coarse-grid CFD-DEM simulations is still lacking due to the huge computational cost. As the particle sizes studied in the relevant studies are usually only equivalent to a few tens of microns, the computational cost attributed by the implementation of coarse-grid simulations of lab-scale devices is still unaffordable. Especially for polydisperse systems, the number of particles corresponding to the same computational domain increases significantly compared to monodisperse systems. It is worth noting that the proposed model still needs to be further validated by comparing the results of coarse-grid CFD-DEM simulations with experimental data in the future.

6. Conclusions

In this work, we developed a drag correction model that can be used in coarse-grid CFD-DEM simulations of the gas–solid systems

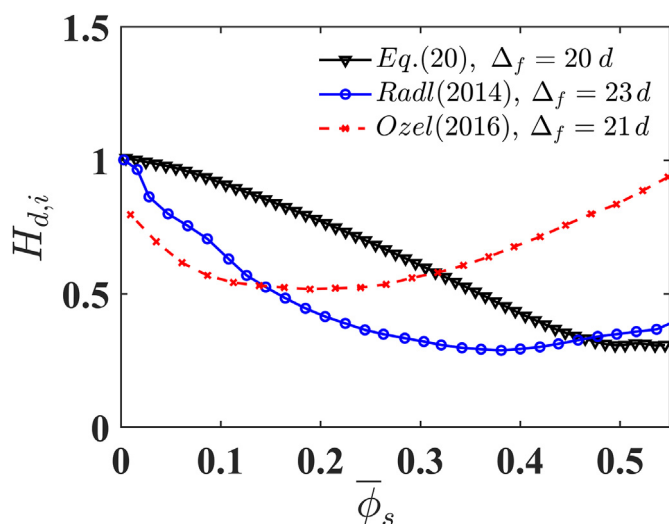


Fig. 11. Comparisons of the drag corrections of Eq. (20) with data from Radl and Sundaresan (2014) and Ozel et al. (2016) in the monodisperse system. The dimensionless filter size is about 20. The dimensionless filtered slip velocity used in Eq. (20) is the median of the data binned by the filtered solid volume fraction.

with general continuous PSDs. Well-resolved CFD-DEM simulations are performed on a monodisperse and several polydisperse cases with different PSDs. Through the processing of the filtering strategy and analysis, the main findings are as follows:

First, for both monodisperse and polydisperse systems, the drag correction of individual particle exhibits a dependence on the filtered solid volume fraction and the dimensionless filtered slip velocity. Second, for polydisperse systems, it is found that the drag correction is correlated with the particle size and surrounding PSD, which is quantified by the ratio of the filter size to the Sauter mean diameter $\frac{d_i}{d}$. The drag correction is sensitive to the variation of $\frac{d_i}{d}$, particularly at low slip velocities. Eventually, based on the filtered solid volume fraction and the filtered slip velocity, a drag correction model for coarse-grid CFD-DEM simulations of the monodisperse system is established. By introducing the new marker $\frac{d_i}{d}$, the effect of PSD is taken into account and a drag correction model for coarse-grid CFD-DEM simulations suitable for general continuous PSD is proposed. A priori analysis indicates that the model exhibits reliable prediction accuracy when the dimensionless filter size ranges from 18 to 30. Accordingly, the developed model is recommended to be applied with a grid size of 18–30 times of the Sauter mean diameter. And the particle size range is preferable within the scope of this study. The corresponding grid number can be reduced by hundreds of times, which can lead to a considerable reduction in computation. The comparison between the models demonstrates that it is desirable to discover and propose new markers in order to more accurately predict the drag correction.

It is worth pointing out that the model is not only customized for coarse-grid CFD-DEM simulations, but can also be readily extended for the coarse-grained CFD-DEM and multi-phase particle-in-cell method simulations (MP-PIC). In addition to the priori analysis, the proposed model still needs to be further validated against experimental data. Incorporation of the model with the

polydisperse coarse-grained model (Lu et al., 2018) may contribute to the large-scale CFD-DEM simulations.

Declaration of competing interest

The authors declare that they have no known competing financial interests or personal relationships that could have appeared to influence the work reported in this paper.

Acknowledgments

This work was supported by the National Natural Science Foundation of China (grant Nos. 91834303 and 21625603).

References

- Agrawal, K., Holloway, W., Milioli, C. C., Milioli, F. E., & Sundaresan, S. (2013). Filtered models for scalar transport in gas–particle flows. *Chemical Engineering Science*, 95, 291–300. <https://doi.org/10.1016/j.ces.2013.03.017>
- Agrawal, K., Loezos, P. N., Syamlal, M., & Sundaresan, S. (2001). The role of meso-scale structures in rapid gas–solid flows. *Journal of Fluid Mechanics*, 445, 151–185. <https://doi.org/10.1017/S0022112001005663>
- Benyahia, S., & Sundaresan, S. (2012). Do we need sub-grid scale corrections for both continuum and discrete gas–particle flow models? *Powder Technology*, 220, 2–6. <https://doi.org/10.1016/j.powtec.2011.10.052>
- Chu, K., Chen, J., & Yu, A. (2016). Applicability of a coarse-grained CFD–DEM model on dense medium cyclone. *Minerals Engineering*, 90, 43–54. <https://doi.org/10.1016/j.mineng.2016.01.020>
- Clarke, D. A., Sederman, A. J., Gladden, L. F., & Holland, D. J. (2018). Investigation of void fraction schemes for use with CFD–DEM simulations of fluidized beds. *Industrial & Engineering Chemistry Research*, 57(8), 3002–3013. <https://doi.org/10.1021/acs.iecr.7b04638>
- Cundall, P. A., & Strack, O. D. (1979). A discrete numerical model for granular assemblies. *Geotechnique*, 29(1), 47–65. <https://doi.org/10.1680/geot.1979.29.1.47>
- Deen, N. G., Annaland, M. V. S., Van der Hoef, M. A., & Kuipers, J. A. M. (2007). Review of discrete particle modeling of fluidized beds. *Chemical Engineering Science*, 62(1–2), 28–44. <https://doi.org/10.1016/j.ces.2006.08.014>
- Di Renzo, A., Cello, F., & Di Maio, F. P. (2011). Simulation of the layer inversion phenomenon in binary liquid–fluidized beds by DEM–CFD with a drag law for polydisperse systems. *Chemical Engineering Science*, 66(13), 2945–2958. <https://doi.org/10.1016/j.ces.2011.03.035>
- Di Renzo, A., Napolitano, E. S., & Di Maio, F. P. (2021). Coarse-grain dem modelling in fluidized bed simulation: A review. *Processes*, 9(2). <https://doi.org/10.3390/pr9020279>. Article 279.
- Gan, J. Q., Zhou, Z. Y., & Yu, A. B. (2016). A GPU-based DEM approach for modelling of particulate systems. *Powder Technology*, 301, 1172–1182. <https://doi.org/10.1016/j.powtec.2016.07.072>
- Gao, X., Li, T., & Rogers, W. A. (2018). Assessment of mesoscale solid stress in coarse-grid TFM simulation of Geldart A particles in all fluidization regimes. *AIChE Journal*, 64(10), 3565–3581. <https://doi.org/10.1002/aic.16341>
- Gao, X., Li, T., Sarkar, A., Lu, L., & Rogers, W. A. (2018). Development and validation of an enhanced filtered drag model for simulating gas–solid fluidization of Geldart A particles in all flow regimes. *Chemical Engineering Science*, 184, 33–51. <https://doi.org/10.1016/j.ces.2018.03.038>
- Geldart, D., Baeyens, J., Pope, D. J., & Van De Wijer, P. (1981). Segregation in beds of large particles at high velocities. *Powder Technology*, 30(2), 195–205. [https://doi.org/10.1016/0032-5910\(81\)80012-5](https://doi.org/10.1016/0032-5910(81)80012-5)
- van der Hoef, M. A., Beetstra, R., & Kuipers, J. A. M. (2005). Lattice-Boltzmann simulations of low-Reynolds-number flow past mono- and bidisperse arrays of spheres: Results for the permeability and drag force. *Journal of Fluid Mechanics*, 528, 233–254. <https://doi.org/10.1017/S0022112004003295>
- Holloway, W., Benyahia, S., Hrenya, C. M., & Sundaresan, S. (2011). Meso-scale structures of bidisperse mixtures of particles fluidized by a gas. *Chemical Engineering Science*, 66(19), 4403–4420. <https://doi.org/10.1016/j.ces.2011.05.037>
- Holloway, W., & Sundaresan, S. (2014). Filtered models for bidisperse gas–particle flows. *Chemical Engineering Science*, 108, 67–86. <https://doi.org/10.1016/j.ces.2013.12.037>
- Hou, Q., Zhou, Z., Curtis, J. S., & Yu, A. (2019). How to generate valid local quantities of particle–fluid flows for establishing constitutive relations. *AIChE Journal*, 65(10), Article e16690. <https://doi.org/10.1002/aic.16690>
- Jajcevic, D., Siegmund, E., Radeke, C., & Khinast, J. G. (2013). Large-scale CFD–DEM simulations of fluidized granular systems. *Chemical Engineering Science*, 98, 298–310. <https://doi.org/10.1016/j.ces.2013.05.014>

- Jiang, Y., Chen, X., Kolehmainen, J., Kevrekidis, I. G., Ozel, A., & Sundaresan, S. (2021). Development of data-driven filtered drag model for industrial-scale fluidized beds. *Chemical Engineering Science*, 230. <https://doi.org/10.1016/j.ces.2020.116235>. Article 116235.
- Joseph, G. G., Lebreiro, J., Hrenya, C. M., & Stevens, A. R. (2007). Experimental segregation profiles in bubbling gas-fluidized beds. *AIChE Journal*, 53(11), 2804–2813. <https://doi.org/10.1002/aic.11282>
- Lan, B., Xu, J., Zhao, P., Zou, Z., Wang, J., & Zhu, Q. (2021). Scale-up effect of residence time distribution of polydisperse particles in continuously operated multiple-chamber fluidized beds. *Chemical Engineering Science*, 244. <https://doi.org/10.1016/j.ces.2021.116809>. Article 116809.
- Lan, B., Xu, J., Zhao, P., Zou, Z., Zhu, Q., & Wang, J. (2020). Long-time coarse-grained CFD-DEM simulation of residence time distribution of polydisperse particles in a continuously operated multiple-chamber fluidized bed. *Chemical Engineering Science*, 219. <https://doi.org/10.1016/j.ces.2020.115599>. Article 115599.
- Lei, H., Liao, J. W., Zhu, L. T., & Luo, Z. H. (2021). CFD-DEM modeling of filtered fluid-particle drag and heat transfer in bidisperse gas-solid flows. *Chemical Engineering Science*, 246. <https://doi.org/10.1016/j.ces.2021.116896>. Article 116896.
- Lei, H., Zhu, L. T., & Luo, Z. H. (2021). Study of filtered interphase heat transfer using highly resolved CFD-DEM simulations. *AIChE Journal*, 67(4), Article e17121. <https://doi.org/10.1002/aic.17121>
- Li, S., Zhao, P., Xu, J., Zhang, L., & Wang, J. (2022). CFD-DEM simulation of polydisperse gas-solid flow of Geldart A particles in bubbling micro-fluidized beds. *Chemical Engineering Science*. <https://doi.org/10.1016/j.ces.2022.117551>. Article 117551.
- Lu, L., Xu, Y., Li, T., & Benyahia, S. (2018). Assessment of different coarse graining strategies to simulate polydisperse gas-solids flow. *Chemical Engineering Science*, 179, 53–63. <https://doi.org/10.1016/j.ces.2018.01.003>
- Milioli, C. C., Milioli, F. E., Holloway, W., Agrawal, K., & Sundaresan, S. (2013). Filtered two-fluid models of fluidized gas-particle flows: New constitutive relations. *AIChE Journal*, 59(9), 3265–3275. <https://doi.org/10.1002/aic.14130>
- Ozel, A., Kolehmainen, J., Radl, S., & Sundaresan, S. (2016). Fluid and particle coarsening of drag force for discrete-parcel approach. *Chemical Engineering Science*, 155, 258–267. <https://doi.org/10.1016/j.ces.2016.08.014>
- Qin, Z., Zhou, Q., & Wang, J. (2019). An EMMS drag model for coarse grid simulation of polydisperse gas–solid flow in circulating fluidized bed risers. *Chemical Engineering Science*, 207, 358–378. <https://doi.org/10.1016/j.ces.2019.06.037>
- Radl, S., & Sundaresan, S. (2014). A drag model for filtered Euler–Lagrange simulations of clustered gas–particle suspensions. *Chemical Engineering Science*, 117, 416–425. <https://doi.org/10.1016/j.ces.2014.07.011>
- Rauchenzauner, S., & Schneiderbauer, S. (2020). A dynamic Spatially Averaged Two-Fluid Model for heat transport in moderately dense gas–particle flows. *Physics of Fluids*, 32(6). <https://doi.org/10.1063/5.0008418>. Article 063307.
- Rong, L. W., Dong, K. J., & Yu, A. B. (2014). Lattice-Boltzmann simulation of fluid flow through packed beds of spheres: Effect of particle size distribution. *Chemical Engineering Science*, 116, 508–523. <https://doi.org/10.1016/j.ces.2014.05.025>
- Sarkar, A., Milioli, F. E., Ozarkar, S., Li, T., Sun, X., & Sundaresan, S. (2016). Filtered sub-grid constitutive models for fluidized gas-particle flows constructed from 3-D simulations. *Chemical Engineering Science*, 152, 443–456. <https://doi.org/10.1016/j.ces.2016.06.023>
- Schneiderbauer, S., Puttinger, S., & Pirker, S. (2013). Comparative analysis of subgrid drag modifications for dense gas-particle flows in bubbling fluidized beds. *AIChE Journal*, 59(11), 4077–4099. <https://doi.org/10.1002/aic.14155>
- Seyed-Ahmadi, A., & Wachs, A. (2020). Microstructure-informed probability-driven point-particle model for hydrodynamic forces and torques in particle-laden flows. *Journal of Fluid Mechanics*, 900. <https://doi.org/10.1017/jfm.2020.453>
- Sundaresan, S., Ozel, A., & Kolehmainen, J. (2018). Toward constitutive models for momentum, species, and energy transport in gas–particle flows. *Annual Review of Chemical And Biomolecular Engineering*, 9, 61–81. <https://doi.org/10.1146/annurev-chembioeng-060817-084025>
- Sun, G., & Grace, J. R. (1990). The effect of particle size distribution on the performance of a catalytic fluidized bed reactor. *Chemical Engineering Science*, 45(8), 2187–2194. [https://doi.org/10.1016/0009-2509\(90\)80094-U](https://doi.org/10.1016/0009-2509(90)80094-U)
- Tirapelle, M., Santomaso, A. C., & Mazzei, L. (2022). CFD-PBE coupled model for size-driven segregation in polydisperse granular flows. *Chemical Engineering Science*, 247. <https://doi.org/10.1016/j.ces.2021.117065>. Article 117065.
- Verma, V., Li, T., & De Wilde, J. (2017). Coarse-grained discrete particle simulations of particle segregation in rotating fluidized beds in vortex chambers. *Powder Technology*, 318, 282–292. <https://doi.org/10.1016/j.powtec.2017.05.037>
- Wang, C. (2013). *High density gas-solids circulating fluidized bed riser and downer reactors*. London: The University of Western Ontario. <https://ir.lib.uwo.ca/etd/1572>.
- Wang, S., & Shen, Y. (2022). Coarse-grained CFD-DEM modelling of dense gas-solid reacting flow. *International Journal of Heat and Mass Transfer*, 184. <https://doi.org/10.1016/j.ijheatmasstransfer.2021.122302>. Article 122302.
- Wu, S. Y., & Baeyens, J. (1998). Segregation by size difference in gas fluidized beds. *Powder Technology*, 98(2), 139–150. [https://doi.org/10.1016/S0032-5910\(98\)00026-6](https://doi.org/10.1016/S0032-5910(98)00026-6)
- Xue, Q., & Fox, R. O. (2014). Reprint of: Multi-fluid CFD modeling of biomass gasification in polydisperse fluidized-bed gasifiers. *Powder Technology*, 265, 23–34. <https://doi.org/10.1016/j.powtec.2014.04.006>
- Xu, J., Qi, H., Fang, X., Lu, L., Ge, W., Wang, X., ... Li, J. (2011). Quasi-real-time simulation of rotating drum using discrete element method with parallel GPU computing. *Particuology*, 9(4), 446–450. <https://doi.org/10.1016/j.partic.2011.01.003>
- Yu, Y., Li, Y., Jiang, M., & Zhou, Q. (2020). Meso-scale drag model designed for coarse-grid Eulerian-Lagrangian simulation of gas-solid flows. *Chemical Engineering Science*, 223. <https://doi.org/10.1016/j.ces.2020.115747>. Article 115747.
- Zhang, Y., Zhao, Y., Lu, L., Ge, W., Wang, J., & Duan, C. (2017). Assessment of polydisperse drag models for the size segregation in a bubbling fluidized bed using discrete particle method. *Chemical Engineering Science*, 160, 106–112. <https://doi.org/10.1016/j.ces.2016.11.028>
- Zhao, J., & Shan, T. (2013). Coupled CFD-DEM simulation of fluid–particle interaction in geomechanics. *Powder Technology*, 239, 248–258. <https://doi.org/10.1016/j.powtec.2013.02.003>
- Zhou, Q., & Wang, J. (2015). CFD study of mixing and segregation in CFB risers: Extension of EMMS drag model to binary gas–solid flow. *Chemical Engineering Science*, 122, 637–651. <https://doi.org/10.1016/j.ces.2014.10.025>
- Zhou, Y. C., Wright, B. D., Yang, R. Y., Xu, B. H., & Yu, A. B. (1999). Rolling friction in the dynamic simulation of sandpile formation. *Physica A: Statistical Mechanics and Its Applications*, 269(2–4), 536–553. [https://doi.org/10.1016/S0378-4371\(99\)00183-1](https://doi.org/10.1016/S0378-4371(99)00183-1)
- Zhu, L. T., Liu, Y. X., Tang, J. X., & Luo, Z. H. (2019). A material-property-dependent sub-grid drag model for coarse-grained simulation of 3D large-scale CFB risers. *Chemical Engineering Science*, 204, 228–245. <https://doi.org/10.1016/j.ces.2019.04.026>
- Zhu, L. T., Ouyang, B., Lei, H., & Luo, Z. H. (2021). Conventional and data-driven modeling of filtered drag, heat transfer, and reaction rate in gas–particle flows. *AIChE Journal*, 67(8), Article e17299. <https://doi.org/10.1002/aic.17299>
- Zhu, L. T., Tang, J. X., & Luo, Z. H. (2020). Machine learning to assist filtered two-fluid model development for dense gas–particle flows. *AIChE Journal*, 66(6), Article e16973. <https://doi.org/10.1002/aic.16973>
- Zhu, H. P., Zhou, Z. Y., Yang, R. Y., & Yu, A. B. (2007). Discrete particle simulation of particulate systems: Theoretical developments. *Chemical Engineering Science*, 62(13), 3378–3396. <https://doi.org/10.1016/j.ces.2006.12.089>